

Article pubs.acs.org/JPCC

Momentum-Resolved Electronic Structures of a Monolayer-MoS₂/ Multilayer-MoSe₂ Heterostructure

Woojoo Lee, Li-Syuan Lu, Wen-Hao Chang,* and Chih-Kang Shih*



Cite This: J. Phys. Chem. C 2021, 125, 16591-16597



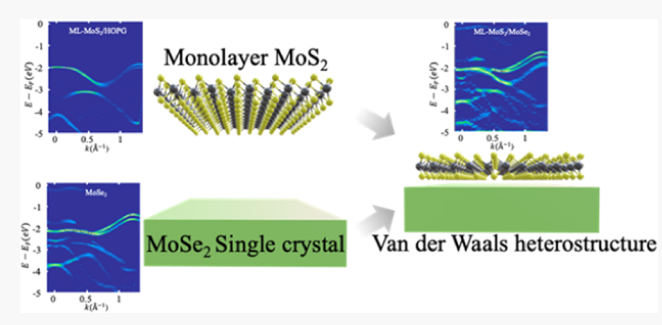
ACCESS I

III Metrics & More

Article Recommendations

Supporting Information

ABSTRACT: By creating a large-scale and highly oriented monolayer-MoS₂/multilayer-MoSe₂ heterostructure with an atomically clean interface, we use angle-resolved photoemission spectroscopy (ARPES) to probe the electronic structure of the created heterostructure and its respective constituents. This comparative study allows us to determine the band offset at the K-point and to reveal k-resolved interlayer hybridization in the Brillouin zone. We further discuss the effect of moiré potential on the state at the Kvalley for MoS₂. We expect that our approach of creating heterostructures and the k-resolved study of the electronic band structure will elucidate how interlayer coupling manifests in



determining the electronic structure formation of transition metal dichalcogenide (TMD) vertical heterostructures.

INTRODUCTION

Designing and creating an electronic band structure in a targeted manner has been a long-term goal in materials science. Recently, it has been realized that van der Waals heterostructures can be a powerful platform for realization of novel quantum phenomena¹⁻⁶ and applications in electronics and nanophotonics.^{7–15} Amid a phenomenal growth of research activities of semiconducting transition metal dichalcogenide (TMD) heterostructures, the progress in direct k-space measurements of TMD heterostructures using angle-resolved photoemission spectroscopy (ARPES) has been slow, despite its critical role in assessing the theoretical models used to predict the electronic structures. To successfully apply ARPES, it is necessary to create the heterostructures that are laterally homogeneous within the probing area. 16-27 Most TMD heterostructures are created using mechanical exfoliation/ stacking methods, which limits the lateral dimension to a few microns. It becomes necessary to use micro-/nano-ARPES to probe the electronic structure in k-space for small samples, ²⁸⁻³² which limits the wide applicability. To overcome this limitation, it is important to develop a large, scalable heterostructure platform that is laterally homogeneous with a well-defined in-plane orientation (namely, single-crystal-like heterojunction).

Here, we report the creation of such a TMD heterostructure platform consisting of a well-aligned MoS2 monolayer on a single-crystal MoSe₂ (referred to as ML-MoS₂/multilayer-MoSe₂ or ML-MoS₂/MoSe₂). This platform enables us to use regular ARPES and observe its electronic structure directly, from which we determine important quantities including the K-valley valence band offset (VBO) and the k-resolved interlayer hybridization between ML-MoS₂ and multilayerMoSe₂. By comparing our experimental observation and density functional theory (DFT) calculations, we illuminate the role of the atomic orbital projection on the k-resolved interlayer hybridization. We further discuss the role of moiré pattern formation on the observed electronic structures.

METHODS

Experimental Details. The regular ARPES measurements of the electronic band structure were performed at room temperature. A helium lamp (21.2 and 40.8 eV) was used as the photon source. Spectra were collected using a Scienta R3000 analyzer. During the helium lamp operation, the pressure was maintained under 6×10^{-10} Torr.

Computational Details. The DFT calculations were performed using the Quantum Espresso package. 33,34 The Perdew-Burke-Ernzerhof (PBE) form of the generalized gradient approximation (GGA) pseudopotential was used within the projector augmented wave (PAW) method and the van der Waals interaction was accounted using the empirical correction proposed by Gimme (DFT-D2).35 The plane-wave basis with a 40 Ry plane-wave cutoff energy was employed. The reciprocal space was sampled by the $10 \times 10 \times 2$ k-mesh for multilayer calculations and $12 \times 12 \times 1$ for monolayer calculation.

Received: May 12, 2021 July 4, 2021 Revised: Published: July 21, 2021





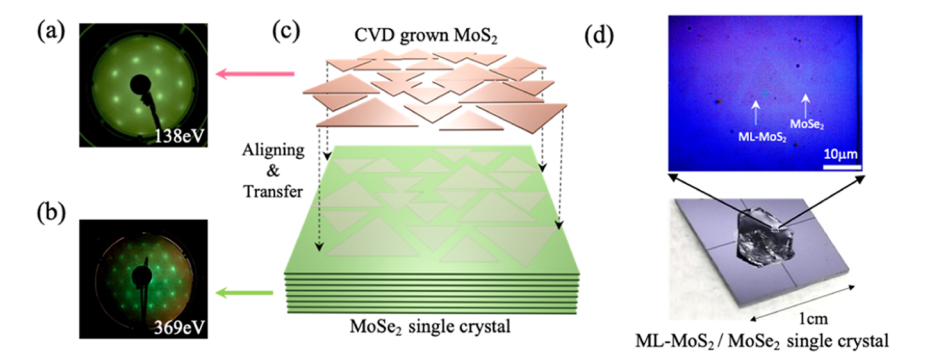


Figure 1. Sample preparation for the TMD heterostructure. A scalable and highly oriented (only twin domains) monolayer MoS₂ sample was first grown on a sapphire substrate via the CVD method and transferred onto a freshly cleaved MoSe₂ single crystal. (a, b) Low-energy electron diffraction (LEED) images of monolayer MoS₂ on highly oriented pyrolytic graphite (HOPG) and the MoSe₂ single crystal, respectively; CVD grown monolayer MoS₂ was transferred onto HOPG for the LEED measurement. (c) Schematic of the sample preparation. (d) Optical image of the sample.

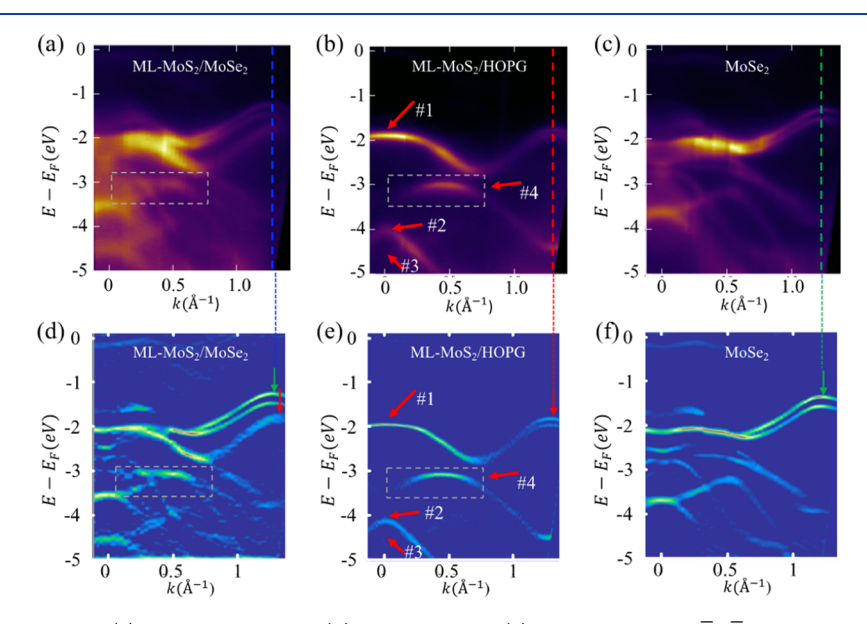


Figure 2. ARPES spectral images of (a) ML-MoS₂/MoSe₂, (b) MoS₂/HOPG, (c) MoSe₂ along the $\overline{\Gamma}$ - \overline{K} direction, measured at 21.2 eV photon energy, and (d-f) corresponding 2D curvature images. The remnant intensity near the Fermi level in (d, f) was yielded by the He-I β light from the helium lamp.

For the heterostructure DFT calculations, we use a 1×1 unit cell with an averaged lattice constant (3.22 Å) between MoS₂ and MoSe₂, consequently, each of them is biaxially strained (~2%). Also, a C7 atomic configuration is used and the interlayer distance between the two different materials is adopted from the relaxed structure of the MoS₂/4 layer MoSe₂ (Mo_{MoS₂}–Mo_{MoSe₂}) distance of 6.39 Å. We note that the strain and stacking configuration can affect the calculated band structure, however, this difference is minor in comparison to the orbital character-dependent hybridization effect. The strained monolayer MoS₂ and 8-layer MoSe₂ band structures are shown in Figure S1.

■ RESULTS AND DISCUSSION

The creation of a large area TMD heterostructure is schematically illustrated in Figure 1c. First, a large-scale and highly oriented MoS₂ monolayer was prepared on a sapphire substrate by a substrate-guided chemical vapor deposition (CVD) growth method.^{23–25} The monolayer orientation can be determined using the edge of the well-aligned triangular flakes (see Supporting Information Figure S2). This

orientation alignment is further confirmed by the low-energy electron diffraction (LEED) pattern after being transferred to the graphite substrate and cleaned in an ultrahigh vacuum (Figure 1a). To obtain a laterally homogeneous heterostructure, the well-aligned ML-MoS2 must cover nearly the entire surface. In our experiment, the monolayer coverage was 80-90%. A cleaved single-crystal MoSe₂ was used as the substrate whose in-plane orientation was determined using LEED prior to transfer (Figure 1b). With the in-plane orientations of both the MoS2 monolayer and the MoSe2 substrate determined, they were stacked under an optical microscope within an accuracy of $\sim 1^{\circ}$ (Figure 1c). The sample transfer follows a standard procedure of two-dimensional (2D) material transfer using the poly(methyl methacrylate) (PMMA) polymer and thermal release tape (see Supporting Information Figure S2 for the detailed procedure). After transfer, the PMMA layers were removed using acetone and the sample was annealed in the UHV chamber at 300 °C overnight, which successfully cleaned the sample surface. We note that the well-aligned ML-MoS2 has an angular fluctuation of 1-2°, which has some bearing on the resulting

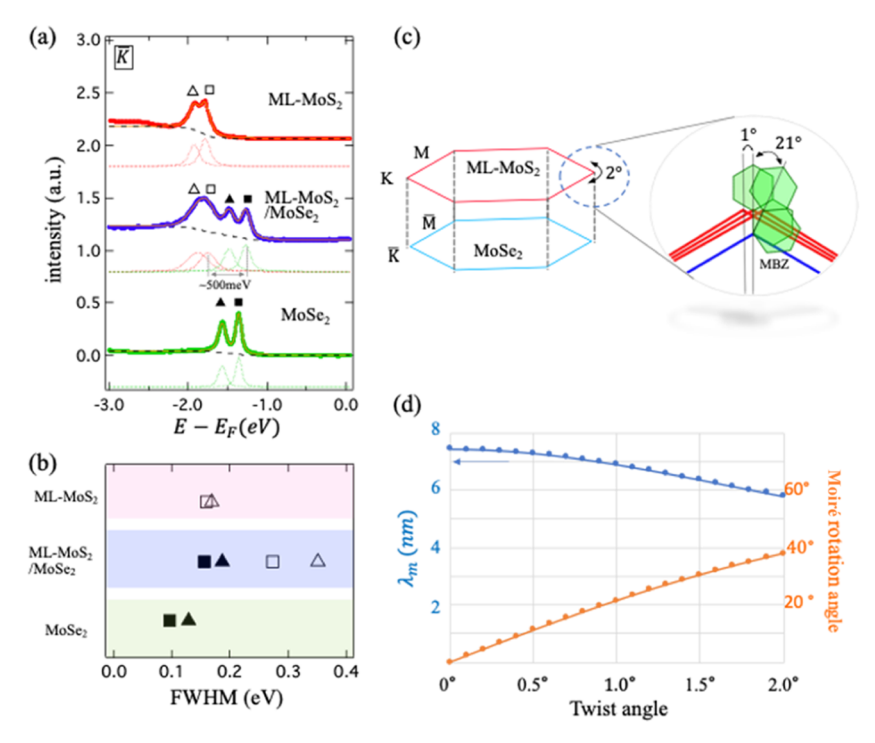


Figure 3. Moiré effect on ML-MoS₂ SO-splitting bands at the *K*-point and band offset. (a) Energy distribution curves at the *K*-point. The Shirley background and Voigt functions are used for the fitting. The *K*-point position of ML-MoS₂/MoSe₂ was assigned between the *K*-point of ML-MoS₂ and MoSe₂. (b) Full width at half-maximum (FWHM) from the fitting. (c) Aligned surface Brillouin zone with a 2° angle fluctuation of ML-MoS₂. The mini Brillouin zone (MBZ) orientation is affected largely by the small-angle variation. (d) Calculated moiré wavelength and moiré rotation angle with respect to the twist angle.

heterostructure spectra. An optical image of the created ML-MoS₂/multilayer-MoSe₂ sample is shown in Figure 1d.

Figure 2a-c shows ARPES band mapping along the Γ -Kdirection for ML-MoS₂/MoSe₂, ML-MoS₂/HOPG, and the cleaved MoSe₂, respectively, using 21.2 eV photons as the excitation source. The respective 2D curvature images are shown below (Figure 2d-f), exhibiting a sharper contrast for individual bands. The 40.8 eV photon source was also used to acquire ARPES spectra. In that case, the spectra exhibit different contrast between individual bands due to the photoionization effect (see Supporting Information Figure S3). The angular alignment between ML-MoS₂ and MoSe₂ can be seen in the 2D constant energy contour near the K-point (see Supporting Information Figure S4). Since the HOPG bands barely interact with ML-MoS2 bands in the current study region, we consider them as intrinsic bands of ML-MoS₂ and investigate how they are hybridized with bulk MoSe2 bands.

We first discuss the electronic structure at the K-valley. Note that ML-MoS₂ and MoSe₂ have a lattice mismatch of ~4% (3.16 vs 3.30 Å), resulting in slightly different locations of K-points for ML-MoS₂ and MoSe₂ (respectively, marked by the red and green arrows in Figure 2). A spin—orbit (SO) splitting of 0.20 eV at the K-valley (green arrow) is well resolved for MoSe₂ either in ML-MoS₂/MoSe₂ (Figure 2a,d) or in the bulk form (Figure 2c,f). On the other hand, an SO splitting of 0.14 eV is resolved for ML-MoS₂ on graphite (Figure 2b,e) but not for ML-MoS₂/MoSe₂ (Figure 2a,d). The energy dispersion curves (EDC) at the K-point for all three cases (ML-MoS₂/MoSe₂, ML-MoS₂/HOPG, and MoSe₂) are displayed in Figure 3a.

One notes that in ML-MoS₂/MoSe₂, the SO splitting of MoSe₂ retains the same value as the case in pure MoSe₂, albeit

with a ~0.1 eV upward shift relative to the Fermi level. Meanwhile, the SO splitting of ML-MoS2 is no longer resolved directly in ML-MoS₂/MoSe₂, although the curve fitting still allows one to distinguish the two SO-splitting peaks (Figure 3a). Also shown in Figure 3b are the values for the full width at half-maximum (FWHM) of the SO split peaks in Figure 3a. One can see that for MoSe₂, the FWHM changes from \sim 0.1 to ~ 0.15 eV in the ML-MoS₂/MoSe₂. By contrast, for ML-MoS₂, the FWHM changes from ~ 0.15 to ~ 0.3 eV. We note that, in the fittings, though the amplitude ratio in SO-splitting bands changes between ML-MoS₂ and ML-MoS₂/MoSe₂, it does not significantly affect the FWHM and so the same conclusion can be drawn. The spectra acquired with the 40.8 eV photon energy yield a similar result (Figure S5). The fact that the SO split bands for MoSe₂ remain well resolved in the heterostructure suggests a good quality of the ML-MoS₂/ MoSe₂ interface. As we discuss below, the extra broadening is likely the result of moiré pattern formation.

For a lattice-mismatched system of ML-MoS₂ on MoSe₂, the moiré pattern with a wavelength of $\lambda_{\rm m}\approx 7$ nm is anticipated near the zero twist angle ($\theta\approx 0^{\circ}$). Note that for this lattice-mismatched system, $\lambda_{\rm m}$ does not change much for a small-angle deviation, however, the orientation of the moiré pattern is extremely sensitive to the twist angle (see Figure 3c,d). For example, with the twist angle changing from $\theta=0$ to 1° , $\lambda_{\rm m}$ changes from 7.4 to 6.9 nm, but the orientation of the moiré pattern changes from 0 to 21° . With an angular fluctuation of the in-plane orientation of $\sim 2^{\circ}$, we anticipate that the moiré pattern orientation would be fluctuating throughout all angles, even though $\lambda_{\rm m}$ experiences a small change. Moreover, with such a large $\lambda_{\rm m}\approx 7$ nm, the moiré Brillouin zone will be very small so that the fine structure of the moiré band structure will be difficult to resolve with the finite k-resolution of the

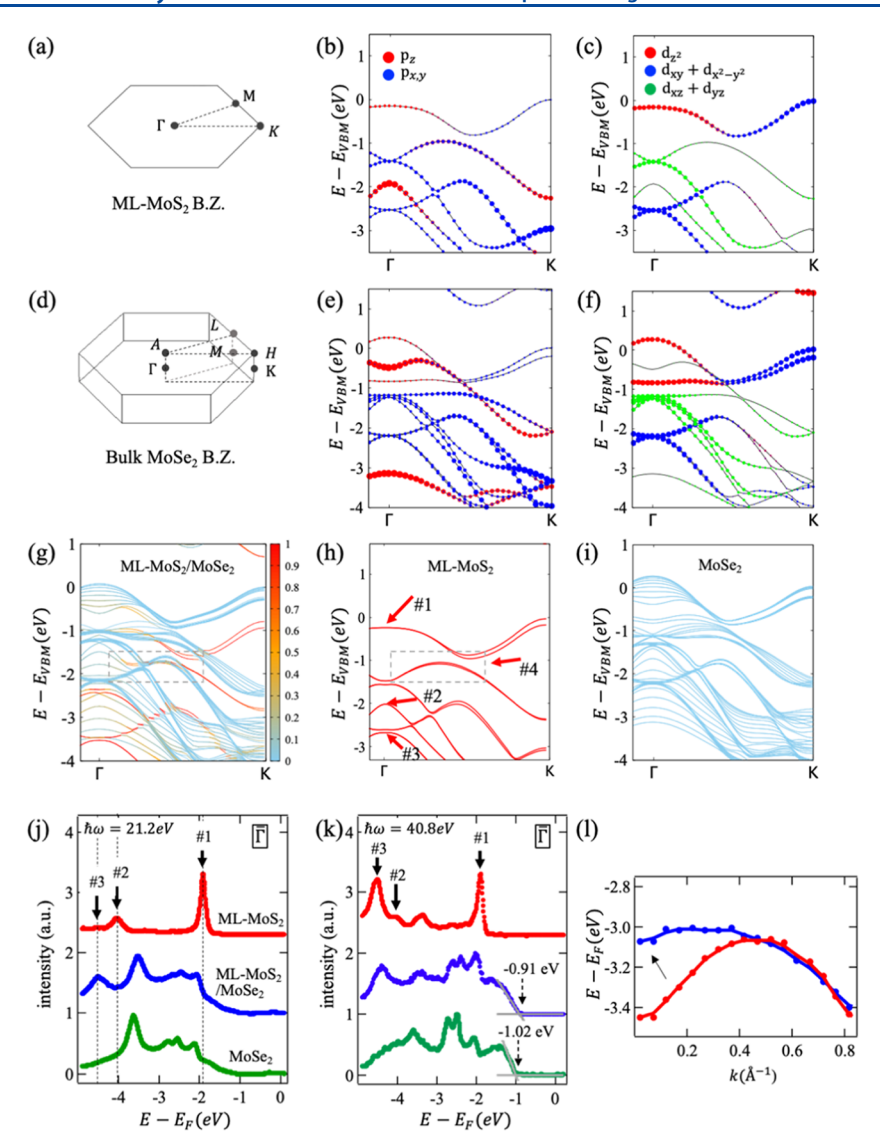


Figure 4. (a–c) Brillouin zones of ML-MoS₂ and atomic orbital projections of its band structure (without SOC), respectively. (d–f) Brillouin zones of bulk MoSe₂ and atomic orbital projections of its band structure (without SOC). (g–i) Calculated electronic band structures by DFT calculations. (j, k) Energy distribution curves at the Γ point acquired with 21.2 and 40.8 eV photon energies, respectively. (l) Hybridization-induced ML-MoS₂ band (red) flattening in ML-MoS₂/MoSe₂ (blue). The peak position was extracted from the ARPES spectra by fitting.

instrument. To the best of our knowledge, direct observation of moiré minibands at the K-point in such small-twisted angle or small lattice-mismatched TMD heterostructures has not been reported, albeit evidence for the miniband formation near the Γ point has been suggested in ref 32. This can be attributed to the fact that the moiré miniband formed with the TMD's parabolic shape valence band in small mini BZ is hard to be distinguished. The case for bilayer graphene is rather different because of a large group velocity associated with the sharp Dirac cone. ³⁸

The above analysis suggests that the effect of the moiré potential modulation can only be observed as an ensemble average in our system. Indirectly, the magnitude of the extra broadening should reflect the amplitude of moiré potential modulation. To quantitatively capture this, however, is nontrivial. Nevertheless, as discussed in the Supporting Information, the moiré modulation primarily leads to an "extra width" in the spectral linewidth instead of a simple Gaussian broadening (Figure S6). Note that the extra broadening in ML-MoS₂ is of the order of 150 meV, while

in MoSe₂ is only 50 meV, reflecting the fact that the moiré pattern has a smaller impact on the underlayer MoSe₂, which is a bulk material. We note that there can be local fluctuations created by impurities or defects at the interface causing the peak broadening. However, this peak broadening will be applied equally to ML-MoS2 peaks in ML-MoS2/HOPG and ML-MoS₂/MoSe₂, since they were prepared in a similar wettransfer method. Furthermore, the electron escape depth of 21.2 eV photon energy is \sim 10 Å, if the fluctuating interface potential was a major factor of the ML-MoS₂ peak broadening in ML-MoS₂/MoSe₂, it should affect the underlying MoSe₂ peak width comparably in the EDC of ML-MoS₂/MoSe₂. However, the 100 meV difference of the FWHM shows that it cannot be explained solely by the impurity-induced broadening. Therefore, it does not contradict to see the origin of the additional broadening as the moiré effect.

The momentum mapping of the electronic structure in ML-MoS₂/MoSe₂ also allows us to determine a K-valley valence band offset (VBO) of \sim 500 meV, as shown in Figure 3a. It is noted that the K-valley valence band maximum (VBM) states

of MoS_2 and $MoSe_2$ are composed primarily of d_{xy} and $d_{x^2-y^2}$ orbitals with weak interlayer coupling, thus there should be little change for these states in the heterostructure. ^{28,30} Consequently, although the *K*-valley VBO was determined for ML-MoS $_2$ and bulk-MoS $_2$ heterostructures, the VBO value should be similar to the case for the ML-MoS $_2$ /ML-MoS $_2$ hetero-bilayer.

We next discuss the k-dependent interlayer hybridization revealed by ARPES. The k-dependence of interlayer hybridization is rooted in the atomic orbitals and the relative energy location between the constituents.³⁹ Shown in Figure 4a-f are Brillouin zones and DFT calculations of the orbital projected band structures (without spin-orbit coupling (SOC)) for ML-MoS₂ and bulk MoSe₂ displayed in the color code. For example, in ML-MoS₂, the states near the VBM change from primarily $d_{x^2-y^2}$, d_{xy} characters at the K-point, where the interlayer hybridization is not expected, to primarily d_{z^2} at the Γ point where strong interlayer hybridization is expected. We notice that though several studies reported band hybridizations on the TMD heterostructure, 28 it was restricted to a low binding energy level. In our work, we investigated the band hybridization at a higher binding energy level to reveal how the electronic band structure of monolayer TMD can be engineered with the help of high-resolution ARPES measure-

In addition, DFT calculations for the band structures of ML-MoS $_2$ /8L-MoSe $_2$, ML-MoS $_2$, and 8L-MoSe $_2$ are displayed in Figure 4g—i respectively. Here, SOC is included in the calculations. For the heterostructure (ML-MoS $_2$ /8L-MoSe $_2$), we use the average lattice constant for ML-MoS $_2$ and MoSe $_2$, corresponding to a slightly stretched ML-MoS $_2$ and compressed MoSe $_2$. Such an artificial strain effect would alter the fine details of ML-MoS $_2$ and MoSe $_2$ band structures and the subsequent band offset at the K-valley (see Supporting Information Figure S7); nevertheless, it can still capture the hybridization effect.

In the band structure of the heterostructure from DFT calculations shown in Figure 4g, the color bar on the right indicates the degree of mixture of states derived from ML-MoS $_2$ and that from MoS $_2$ multilayers. We label four key features (#1–#4) in the MoS $_2$ monolayer band structure for a detailed discussion.

Shown in Figure 4j,k are EDCs for ML-MoS₂/MoSe₂ and its constituents at the $\overline{\Gamma}$ point acquired with He-I (21.2 eV) and He-II (40.8 eV), respectively. In a bulk MoSe₂, the states formed of out-of-plane orbitals (Mo $4d_z^2$, Se $4p_z$) create bulk continuum states, which were more easily observed with the 40.8 eV photon energy near the $\overline{\Gamma}$ point VBM and around -4 eV (see Figure 4k, the lowest panel); it shows a relatively weak and continuous signal intensity. 16,40,41 On the other hand, the states formed of in-plane orbitals $(d_{x^2-y^2}, d_{xy}, p_x, p_y)$ interact weakly with neighboring layers and thus become nearly degenerate, which show sharp and strong peaks in the obtained spectra. In the current measurement, the bulk-MoSe₂ VBM at the $\overline{\Gamma}$ point is located 300 meV higher than the \overline{K} point VBM. In contrast to the bulk MoSe₂, the bands in ML-MoS₂ show well-defined dispersion without continuum states. In the spectra, the 21.2 eV light shows a higher photoionization cross section on the S 3p orbital than the 40.8 eV light, so it causes a different intensity contrast. 42,43 The Γ point VBM is located 130 meV below the K-point VBM.

Note that in the ML-MoS₂/MoSe₂ ARPES spectra, the MoSe₂-derived sharp features are replicated very well except

for a 0.1 eV rigid upward shift observed at the $\overline{\Gamma}$ and \overline{K} -valley. This upward rigid shift is attributed to the change in work function with an ML-MoS2 overlayer. Unlike the preserved MoSe₂ feature in ML-MoS₂/MoSe₂, at the $\bar{\Gamma}$ point, the sharp feature #1 of ML-MoS₂ is merged into the continuum near the VBM in ML-MoS₂/MoSe₂. This is not surprising since this state (feature #1) mainly contains a majority of d_z² orbitals mixed with a minority of p₂ orbitals and strong hybridization is expected. 16,44 Similarly, feature #2 (containing primarily pz mixed with a minority of $d_{xz, yz}$) in ML-MoS₂ merges into the continuum states due to hybridization. Such hybridizations are also reflected in the DFT calculations. By contrast, feature #3 (containing mainly $d_{x^2-y^2}$, d_{xy} mixed with minority p_x , p_y as shown in Figure 4c,d) in ML-MoS₂ is observed in ML-MoS₂/ MoSe₂ spectra acquired with the He-II light (Figure 4k), indicating no hybridization effect. The absence of hybridization is also shown in the DFT calculations. Interestingly, for the spectra acquired using the He-I light, this feature is not observed in ML-MoS₂ but is observed in ML-MoS₂/MoSe₂. It cannot simply be a difference in the photoionization effect since the same should apply to the feature in ML-MoS₂/ MoSe₂. Here, we suggest that this is due to a final state effect. In ML-MoS₂/HOPG, the HOPG band structure may not provide accessible final states when using 21.2 eV photon energy (see also Figure S8). On the other hand, in ML-MoS₂/ MoSe₂, the MoSe₂ bulk band structure provides accessible final states for feature #3. This scenario can be further supported by looking over bulk MoS₂ ARPES spectra, in which feature #3 is observed in spectra acquired using both the He-I and the He-II light (Figure S9).

Feature #4 characterizes the band structure across an extended k-space as labeled by the dashed box in the ARPES spectra, as shown in Figure 2b,e and the calculation shown in Figure 4h. For this feature, the ML-MoS $_2$ /MoSe $_2$ calculation shows that this band is hybridized with the MoSe $_2$ derived states and the original dispersion becomes significantly altered. Indeed, this is observed experimentally where the highly dispersive character in ML-MoS $_2$ is flattened out in the heterostructure across the k-space between $k_{\parallel} = 0$ and $0.6 \, \text{Å}^{-1}$ (Figure 4l). The evolution of these four features (#1–#4) changing from ML-MoS $_2$ to ML-MoS $_2$ /MoSe $_2$ firmly establishes the k-dependence hybridization between ML-MoS $_2$ and the underlying MoSe $_2$ bulk is rooted in the characters of projected atomic orbitals.

In summary, by transferring a large area ML-MoS2 with a well-aligned in-plane orientation onto a cleaved single-crystal MoSe₂, we create an ML-MoS₂/multilayer-MoSe₂ heterostructure. This platform allows us to use angle-resolved photoelectron spectroscopy to probe the electronic structures of the heterostructure and its constituents (i.e., ML-MoS₂ and bulk MoSe₂) in k-space. This comparative study enables us to determine a valence band offset at the K-valley of 0.5 eV and to reveal k-dependent hybridization effects. Depending on their atomic orbital characters, we find that the ML-MoS₂ derived states near the zone center can either be fully merged into the MoSe₂-derived continuum or retain their original character in the ML-MoS₂. In addition, a hybridized band in an extended kspace (from $k_{\parallel} = 0$ to 0.6 Å⁻¹ along the $\Gamma - K$ direction) is observed with its dispersion significantly altered from that in the ML-MoS₂. We further reveal indirect evidence for the formation of the moiré pattern on the spectra at the K-point. We anticipate this method to create a large area homogeneous TMD heterostructure that can be adopted to create a diverse set of TMD heterostructures and enable *k*-space probe of the electronic structures in vertically stacked vdW heterostructures for intriguing science such as electron dynamics, exciton dynamics, exciton condensation, and quantum phases. ^{27,46–48}

ASSOCIATED CONTENT

Supporting Information

The Supporting Information is available free of charge at https://pubs.acs.org/doi/10.1021/acs.jpcc.1c04219.

Details of the sample preparation; additional ARPES data; analysis of the moiré potential effect; and DFT calculations of artificially strained TMDs (PDF)

AUTHOR INFORMATION

Corresponding Authors

Wen-Hao Chang — Department of Electrophysics, National Chiao Tung University, Hsinchu 30010, Taiwan; Research Center for Applied Sciences, Academia Sinica, Taipei 11529, Taiwan; Center for Emergent Functional Matter Science (CEFMS), National Chiao Tung University, Hsinchu 30010, Taiwan; orcid.org/0000-0003-4880-6006; Email: whchang@mail.nctu.edu.tw

Chih-Kang Shih — Department of Physics, The University of Texas at Austin, Austin, Texas 78712, United States;
Orcid.org/0000-0003-2734-7023; Email: shih@physics.utexas.edu

Authors

Woojoo Lee – Department of Physics, The University of Texas at Austin, Austin, Texas 78712, United States

Li-Syuan Lu – Department of Electrophysics, National Chiao Tung University, Hsinchu 30010, Taiwan

Complete contact information is available at: https://pubs.acs.org/10.1021/acs.jpcc.1c04219

Notes

The authors declare no competing financial interest.

■ ACKNOWLEDGMENTS

This research was primarily supported by the National Science Foundation through the Center for Dynamics and Control of Materials: an NSF MRSEC under Cooperative Agreement No. DMR-1720595. This research was also supported with grants from the Welch Foundation (F-1672), the US National Science Foundation (DMR-1808751), and the US Airforce (FA2386-18-1-4097). W.-H.C. acknowledges the support of the Ministry of Science and Technology of Taiwan (MOST-107-2112-M-009-024-MY3 and MOST-108-2119-M-009-011-MY3) and from the Center for Emergent Functional Matter Science (CEFMS) of NCTU supported by the Ministry of Education of Taiwan. The authors acknowledge the Texas Advanced Computing Center (TACC) at The University of Texas at Austin for providing HPC resources.

REFERENCES

- (1) Cotlet, O.; Zeytinoğlu, S.; Sigrist, M.; Demler, E.; Imamoğlu, A. Superconductivity and Other Collective Phenomena in a Hybrid Bose-Fermi Mixture Formed by a Polariton Condensate and an Electron System in Two Dimensions. *Phys. Rev. B* **2016**, 93, No. 054510.
- (2) Basov, D. N.; Fogler, M. M.; Garcia de Abajo, F. J. Polaritons in van Der Waals Materials. *Science* **2016**, *354*, aag1992.

- (3) Wu, F.; Lovorn, T.; Tutuc, E.; MacDonald, A. H. Hubbard Model Physics in Transition Metal Dichalcogenide Moiré Bands. *Phys. Rev. Lett.* **2018**, *121*, No. 026402.
- (4) Cao, Y.; Fatemi, V.; Fang, S.; Watanabe, K.; Taniguchi, T.; Kaxiras, E.; Jarillo-Herrero, P. Unconventional Superconductivity in Magic-Angle Graphene Superlattices. *Nature* **2018**, *556*, 43–50.
- (5) Cao, Y.; Fatemi, V.; Demir, A.; Fang, S.; Tomarken, S. L.; Luo, J. Y.; Sanchez-Yamagishi, J. D.; Watanabe, K.; Taniguchi, T.; Kaxiras, E.; et al. Correlated Insulator Behaviour at Half-Filling in Magic-Angle Graphene Superlattices. *Nature* **2018**, *556*, 80–84.
- (6) Tang, Y.; Li, L.; Li, T.; Xu, Y.; Liu, S.; Barmak, K.; Watanabe, K.; Taniguchi, T.; MacDonald, A. H.; Shan, J.; et al. Simulation of Hubbard Model Physics in WSe 2 /WS 2 Moiré Superlattices. *Nature* **2020**, *579*, 353–358.
- (7) Geim, A. K.; Grigorieva, I. V. Van Der Waals Heterostructures. *Nature* **2013**, 499, 419–425.
- (8) Xu, X.; Yao, W.; Xiao, D.; Heinz, T. F. Spin and Pseudospins in Layered Transition Metal Dichalcogenides. *Nat. Phys.* **2014**, *10*, 343–350
- (9) Koppens, F. H. L.; Mueller, T.; Avouris, P.; Ferrari, A. C.; Vitiello, M. S.; Polini, M. Photodetectors Based on Graphene, Other Two-Dimensional Materials and Hybrid Systems. *Nat. Nanotechnol.* **2014**, *9*, 780–793.
- (10) Xia, F.; Wang, H.; Xiao, D.; Dubey, M.; Ramasubramaniam, A. Two-Dimensional Material Nanophotonics. *Nat. Photonics* **2014**, *8*, 899–907.
- (11) Lotsch, B. V. Vertical 2D Heterostructures. *Annu. Rev. Mater.* Res. **2015**, 45, 85–109.
- (12) Mak, K. F.; Shan, J. Photonics and Optoelectronics of 2D Semiconductor Transition Metal Dichalcogenides. *Nat. Photonics* **2016**, *10*, 216–226.
- (13) Novoselov, K. S.; Mishchenko, A.; Carvalho, A.; Neto, A. H. C. 2D Materials and van Der Waals Heterostructures. *Science* **2016**, *353*, No. aac9439.
- (14) Manzeli, S.; Ovchinnikov, D.; Pasquier, D.; Yazyev, O. V.; Kis, A. 2D Transition Metal Dichalcogenides. *Nat. Rev. Mater.* **2017**, *2*, No. 17033.
- (15) Rivera, P.; Yu, H.; Seyler, K. L.; Wilson, N. P.; Yao, W.; Xu, X. Interlayer Valley Excitons in Heterobilayers of Transition Metal Dichalcogenides. *Nat. Nanotechnol.* **2018**, *13*, 1004–1015.
- (16) Zhang, Y.; Chang, T.-R.; Zhou, B.; Cui, Y.-T.; Yan, H.; Liu, Z.; Schmitt, F.; Lee, J.; Moore, R.; Chen, Y.; et al. Direct Observation of the Transition from Indirect to Direct Bandgap in Atomically Thin Epitaxial MoSe2. *Nat. Nanotechnol.* **2014**, *9*, 111–115.
- (17) Mo, S.-K.; Hwang, C.; Zhang, Y.; Fanciulli, M.; Muff, S.; Hugo Dil, J.; Shen, Z.-X.; Hussain, Z. Spin-Resolved Photoemission Study of Epitaxially Grown MoSe2and WSe2 Thin Films. *J. Phys.: Condens. Matter* **2016**, 28, No. 454001.
- (18) Grubišić Čabo, A.; Miwa, J. A.; Grønborg, S. S.; Riley, J. M.; Johannsen, J. C.; Cacho, C.; Alexander, O.; Chapman, R. T.; Springate, E.; Grioni, M.; et al. Observation of Ultrafast Free Carrier Dynamics in Single Layer MoS2. *Nano Lett.* **2015**, *15*, 5883–5887.
- (19) Ulstrup, S.; Čabo, A. G.; Miwa, J. A.; Riley, J. M.; Grønborg, S. S.; Johannsen, J. C.; Cacho, C.; Alexander, O.; Chapman, R. T.; Springate, E.; et al. Ultrafast Band Structure Control of a Two-Dimensional Heterostructure. *ACS Nano* **2016**, *10*, 6315–6322.
- (20) Ulstrup, S.; Čabo, A. G.; Biswas, D.; Riley, J. M.; Dendzik, M.; Sanders, C. E.; Bianchi, M.; Cacho, C.; Matselyukh, D.; Chapman, R. T.; et al. Spin and Valley Control of Free Carriers in Single-Layer WS2. *Phys. Rev. B* **2017**, *95*, No. 041405.
- (21) Liu, F.; Ziffer, M. E.; Hansen, K. R.; Wang, J.; Zhu, X. Direct Determination of Band-Gap Renormalization in the Photoexcited Monolayer MoS 2. *Phys. Rev. Lett.* **2019**, *122*, No. 246803.
- (22) Aeschlimann, S.; Rossi, A.; Chávez-Cervantes, M.; Krause, R.; Arnoldi, B.; Stadtmüller, B.; Aeschlimann, M.; Forti, S.; Fabbri, F.; Coletti, C.; et al. Direct Evidence for Efficient Ultrafast Charge Separation in Epitaxial WS2/Graphene Heterostructures. *Sci. Adv.* 2020, 6, No. eaay0761.

- (23) Yu, H.; Liao, M.; Zhao, W.; Liu, G.; Zhou, X. J.; Wei, Z.; Xu, X.; Liu, K.; Hu, Z.; Deng, K.; et al. Wafer-Scale Growth and Transfer of Highly-Oriented Monolayer MoS2 Continuous Films. *ACS Nano* **2017**, *11*, 12001–12007.
- (24) Aljarb, A.; Cao, Z.; Tang, H.-L.; Huang, J.-K.; Li, M.; Hu, W.; Cavallo, L.; Li, L.-J. Substrate Lattice-Guided Seed Formation Controls the Orientation of 2D Transition-Metal Dichalcogenides. *ACS Nano* **2017**, *11*, 9215–9222.
- (25) Hsu, W.-F.; Lu, L.-S.; Kuo, P.-C.; Chen, J.-H.; Chueh, W.-C.; Yeh, H.; Kao, H.-L.; Chen, J.-S.; Chang, W.-H. Monolayer MoS2 Enabled Single-Crystalline Growth of AlN on Si(100) Using Low-Temperature Helicon Sputtering. ACS Appl. Nano Mater. 2019, 2, 1964—1969.
- (26) Zhao, W.; Huang, Y.; Shen, C.; Li, C.; Cai, Y.; Xu, Y.; Rong, H.; Gao, Q.; Wang, Y.; Zhao, L.; et al. Electronic Structure of Exfoliated Millimeter-Sized Monolayer WSe2 on Silicon Wafer. *Nano Res.* **2019**, 12, 3095–3100.
- (27) Liu, F.; Li, Q.; Zhu, X.-Y. Direct Determination of Momentum-Resolved Electron Transfer in the Photoexcited van Der Waals Heterobilayer WS2/MoS2. *Phys. Rev. B* **2020**, *101*, No. 201405.
- (28) Wilson, N. R.; Nguyen, P. V.; Seyler, K.; Rivera, P.; Marsden, A. J.; Laker, Z. P. L.; Constantinescu, G. C.; Kandyba, V.; Barinov, A.; Hine, N. D. M.; et al. Determination of Band Offsets, Hybridization, and Exciton Binding in 2D Semiconductor Heterostructures. *Sci. Adv.* 2017, 3. No. e1601832.
- (29) Henck, H.; Ben Aziza, Z.; Pierucci, D.; Laourine, F.; Reale, F.; Palczynski, P.; Chaste, J.; Silly, M. G.; Bertran, F.; Le Fèvre, P.; et al. Electronic Band Structure of Two-Dimensional WS 2 / Graphene van Der Waals Heterostructures. *Phys. Rev. B* **2018**, *97*, No. 155421.
- (30) Nguyen, P. V.; Teutsch, N. C.; Wilson, N. P.; Kahn, J.; Xia, X.; Graham, A. J.; Kandyba, V.; Giampietri, A.; Barinov, A.; Constantinescu, G. C.; et al. Visualizing Electrostatic Gating Effects in Two-Dimensional Heterostructures. *Nature* **2019**, *572*, 220–223.
- (31) Ulstrup, S.; Koch, R. J.; Singh, S.; McCreary, K. M.; Jonker, B. T.; Robinson, J. T.; Jozwiak, C.; Rotenberg, E.; Bostwick, A.; Katoch, J.; et al. Direct Observation of Minibands in a Twisted Graphene/WS2 Bilayer. *Sci. Adv.* **2020**, *6*, No. eaay6104.
- (32) Xie, S.; Faeth, B. D.; Tang, Y.; Li, L.; Parzyck, C. T.; Chowdhury, D.; Zhang, Y.-H.; Jozwiak, C.; Bostwick, A.; Rotenberg, E. et al. Direct Observation of Distinct Minibands in Moire Superlattices. arXiv:2010.07806 [cond-mat], 2020.
- (33) Giannozzi, P.; Baroni, S.; Bonini, N.; Calandra, M.; Car, R.; Cavazzoni, C.; Ceresoli, D.; Chiarotti, G. L.; Cococcioni, M.; Dabo, I.; et al. QUANTUM ESPRESSO: A Modular and Open-Source Software Project for Quantum Simulations of Materials. *J. Phys.: Condens. Matter* 2009, 21, No. 395502.
- (34) Giannozzi, P.; Andreussi, O.; Brumme, T.; Bunau, O.; Nardelli, M. B.; Calandra, M.; Car, R.; Cavazzoni, C.; Ceresoli, D.; Cococcioni, M.; et al. Advanced Capabilities for Materials Modelling with Quantum ESPRESSO. *J. Phys.: Condens. Matter* **2017**, 29, No. 465901.
- (35) Grimme, S. Semiempirical GGA-type density functional constructed with a long-range dispersion correction. *J. Comput. Chem.* **2006**, 27, 1787–1799.
- (36) Lu, N.; Guo, H.; Zhuo, Z.; Wang, L.; Wu, X.; Cheng Zeng, X. Twisted MX 2 /MoS 2 Heterobilayers: Effect of van Der Waals Interaction on the Electronic Structure. *Nanoscale* **2017**, *9*, 19131–19138.
- (37) Zhang, C.; Chuu, C.-P.; Ren, X.; Li, M.-Y.; Li, L.-J.; Jin, C.; Chou, M.-Y.; Shih, C.-K. Interlayer Couplings, Moiré Patterns, and 2D Electronic Superlattices in MoS2/WSe2 Hetero-Bilayers. *Sci. Adv.* **2017**, *3*, No. e1601459.
- (38) Lisi, S.; Lu, X.; Benschop, T.; de Jong, T. A.; Stepanov, P.; Duran, J. R.; Margot, F.; Cucchi, I.; Cappelli, E.; Hunter, A.; et al. Observation of Flat Bands in Twisted Bilayer Graphene. *Nat. Phys.* **2020**, *17*, 189–193.
- (39) Komsa, H.-P.; Krasheninnikov, A. V. Electronic Structures and Optical Properties of Realistic Transition Metal Dichalcogenide

- Heterostructures from First Principles. Phys. Rev. B 2013, 88, No. 085318.
- (40) Mahatha, S. K.; Patel, K. D.; Menon, K. S. R. Electronic Structure Investigation of MoS 2 and MoSe 2 Using Angle-Resolved Photoemission Spectroscopy and Ab Initio Band Structure Studies. *J. Phys.: Condens. Matter* **2012**, 24, No. 475504.
- (41) Jin, W.; Yeh, P.-C.; Zaki, N.; Zhang, D.; Sadowski, J. T.; Al-Mahboob, A.; van der Zande, A. M.; Chenet, D. A.; Dadap, J. I.; Herman, I. P.; et al. Direct Measurement of the Thickness-Dependent Electronic Band Structure of MoS2 Using Angle-Resolved Photoemission Spectroscopy. *Phys. Rev. Lett.* 2013, 111, No. 106801.
- (42) Damascelli, A. Angle-Resolved Photoemission Studies of the Cuprate Superconductors. *Rev. Mod. Phys.* **2003**, *75*, 473–541.
- (43) Yeh, J. J.; Lindau, I. Atomic Subshell Photoionization Cross Sections and Asymmetry Parameters: $1 \le Z \le 103$. At. Data Nucl. Data Tables 1985, 32, 1–155.
- (44) Miwa, J. A.; Ulstrup, S.; Sørensen, S. G.; Dendzik, M.; Čabo, A. G.; Bianchi, M.; Lauritsen, J. V.; Hofmann, P. Electronic Structure of Epitaxial Single-Layer MoS2. *Phys. Rev. Lett.* **2015**, *114*, No. 046802.
- (45) Hüfner, S.; Photoelectron Spectroscopy (Springer: Berlin) 1995.
- (46) Ovesen, S.; Brem, S.; Linderälv, C.; Kuisma, M.; Korn, T.; Erhart, P.; Selig, M.; Malic, E. Interlayer Exciton Dynamics in van Der Waals Heterostructures. *Commun. Phys.* **2019**, *2*, No. 23.
- (47) Wang, Z.; Rhodes, D. A.; Watanabe, K.; Taniguchi, T.; Hone, J. C.; Shan, J.; Mak, K. F. Evidence of High-Temperature Exciton Condensation in Two-Dimensional Atomic Double Layers. *Nature* **2019**, *574*, 76–80.
- (48) Wang, J.; Ardelean, J.; Bai, Y.; Steinhoff, A.; Florian, M.; Jahnke, F.; Xu, X.; Kira, M.; Hone, J.; Zhu, X.-Y. Optical Generation of High Carrier Densities in 2D Semiconductor Heterobilayers. *Sci. Adv.* **2019**, *5*, No. eaax0145.